Structure of heavy-metal sorbed birnessite: Part 2. Results from electron diffraction

VICTOR A. DRITS,[1,2] BRUNO LANSON,[1,*] CATHERINE BOUGEROL-CHAILLOUT,[3] ANATOLI I. GORSHKOV,[4] AND ALAIN MANCEAU[1]

[1]Environmental Geochemistry Group, LGIT, Maison des Géosciences, BP53, University of Grenoble-CNRS, 38041 Grenoble Cedex 9, France
[2]Geological Institute, Russian Academy of Sciences, 7 Pyzhevsky street, 109017 Moscow, Russia
[3]Laboratory of Crystallography, CNRS, BP166, 38042 Grenoble Cedex 9, France
[4]Institute of Ore Mineralogy (IGEM), Russian Academy of Sciences, 35 Staromonetny street, 109017 Moscow, Russia

ABSTRACT

Selected-area electron diffraction (SAED) and energy-dispersive analysis were used to study the structure of synthetic heavy-metal sorbed birnessites (MeBi). Samples were prepared by equilibrating a suspension of Na-rich buserite (NaBu) at pH 4 in the presence of various heavy metal cations (Me), including Pb, Cd, Zn, and Cu.

Five main types of SAED patterns were observed. Types I and II were observed only for ZnBi micro-crystals, and they both consist of two super-cell reflection networks related by a mirror plane parallel to the $\mathbf{a}^*$-$\mathbf{c}^*$ plane. In direct space, these twinned networks correspond to hexagonal supercells with $A_H = B_H = \sqrt{7}b/\sqrt{3}$, and $A_H = B_H = \sqrt{7}b$, for ZnBi type I and II, respectively. The supercells in the two varieties result from an ordered distribution of vacant layer octahedra capped by interlayer Zn in ZnBi layers. This distribution is described by a hexagonal cell with $A_H = \sqrt{7}b$. In ZnBi micro-crystals of type I, interstratified twinned right- and left-handed fragments are similar to chalcophanite ($ZnMn_3O_7 \cdot 3H_2O$; Wadsley 1955; Post and Appleman 1988), and distributions of vacant layer octahedra from adjacent layers are regularly shifted with respect to each other by 1/3 of the long diagonal of the hexagonal layer unit cell. In ZnBi micro-crystals of type II, distributions of vacant layer octahedra are not regularly shifted from one layer to the adjacent one.

SAED patterns of types III and IV occur for PbBi, ZnBi, and CdBi micro-crystals and contain super-cell reflections distributed parallel to $[100]^*$ with a periodicity that is not commensurate with that of the MeBi sub-structure ($a^*/2.15$ and $a^*/5.25$, respectively). The super-cell reflections result from the ordered distribution within MeBi layers of vacant layer sites capped by Me as pairs along the $\mathbf{a}$ axis. Within each pair, vacant sites are separated by $2a$ for type III, and by $5a$ for type IV. In one-layer monoclinic structures, the apparent incommensurability arises from the $+\mathbf{a}/3$ shift between adjacent layers having a similar one-dimensional periodic distribution of interlayer Me located above and below vacant octahedra sharing three corners with Mn_{layer} octahedra (TC sites). Tetrahedral coordination of these Me cations in TC sites, as in ZnBi, leads to the formation of strong H-bonds between adjacent layers. A similar incommensurate effect occurs in one-layer hexagonal MeBi if octahedrally coordinated Me cations periodically distributed along the $\mathbf{a}$ axis are located above and/or below empty tridentate cavities sharing three edges with Mn_{layer} octahedra (^{VI}TE sites, PbBi).

SAED patterns of type V contain only sub-cell reflections and were observed mostly for PbBi and CuBi micro-crystals. Three different conditions can lead to the absence of super-cell reflections: (1) a low amount of sorbed Me (PbBi); (2) the presence of Me having a scattering power similar to that of Mn on a single side of vacant layer sites (CuBi); or (3) a random distribution of interlayer species.

INTRODUCTION

Buserite and birnessite are layered hydrous Mn oxides, the layers of which are built of edge-sharing Mn octahedra. Hydrated cations are present in their interlayer spaces to compensate the negative layer charge that arises from the presence of heterovalent Mn and/or vacant sites in the octahedral layers. Because buserite and birnessite can fix heavy metals (Co, Pb, Cd, Cu, Zn, …) in contaminated soils and aqueous systems (Tay-

lor and McKenzie 1966; McKenzie 1967, 1980; Burns and Burns 1976; Bendell-Young and Harvey 1992; Manceau et al. 2000 and references therein), it is essential to determine the structure of heavy-metal sorbed birnessites (MeBi).

Selected-area electron diffraction (SAED) has often been used, sometimes to complement X-ray diffraction (XRD), to study the structure of birnessite and especially to reveal the super-cell periodicities in these phyllomanganates (Post and Veblen 1990; Manceau et al. 1992; Kuma et al. 1994; Drits et al. 1997, 1998). However, the origin of super-cell reflections

* E-mail: Bruno.Lanson@obs.ujf-grenoble.fr

observed in SAED patterns of natural and synthetic birnessites has long remained unclear. Giovanoli et al. (1970) described super-cell reflections of high-pH Na-rich synthetic birnessite, hereafter referred to as NaBi, and attributed them to ordering of vacant layer octahedra capped by interlayer cations as in chalcophanite (Wadsley 1955; Post and Appleman 1988). The same interpretation was proposed by Chukhrov et al. (1978) for a Ca-rich birnessite sample, and by Kuma et al. (1994) for synthetic NaBi samples exchanged with different monovalent and divalent cations. In contrast, Post and Veblen (1990) suggested that high-pH synthetic birnessites consist of vacancy-free layers and, therefore, that super-cell reflections more likely result from an ordered distribution of interlayer cations. This conclusion was supported by the contrasting distributions of super-cell reflections observed for NaBi and Mg-exchanged birnessite. However, in their structural model, Mg^{2+} cations are located almost above/below layer octahedral sites (Post and Veblen 1990), and Manceau et al. (1992) showed that this position may be occupied only if underlying octahedral sites are vacant.

New insight into this problem was provided by Drits et al. (1997) and Silvester et al. (1997). Using XRD, SAED, extended X-ray absorption fine structure spectroscopy (EXAFS), and solution chemistry, these authors demonstrated that NaBi consists of vacancy-free layers and that super-cell reflections observed in its SAED patterns result from an ordered distribution of interlayer cations. In contrast, low-pH synthetic birnessites (HBi) resulting from the low-pH equilibration of Na-rich buserite (NaBu) contain significant numbers of vacant layer sites capped by interlayer Mn cations ($Mn_{interlayer}$), but their SAED patterns are either devoid of super-cell reflections or contain extremely faint super-cell reflections (Drits et al. 1997; Manceau et al. 1997; Silvester et al. 1997). Indeed, systematic location of $Mn_{interlayer}$ either above or below vacant layer sites induces a low electrostatic potential contrast between occupied and vacant octahedral layer sites, and the intensity of super-cell reflections is strongly decreased even if vacant layer sites are regularly distributed (Drits et al. 1997; Lanson et al. 2000).

In the present article, SAED and energy-dispersive analysis (EDA) were used to determine the origin of the different super-cell reflection distributions observed for individual micro-crystals of heavy-metal sorbed birnessites equilibrated at pH 4. The sub-structure of these MeBi samples and, in particular, their layer stacking modes, the nature and content of stacking faults, the amounts of vacant layer sites and the location, coordination and amounts of interlayer cations ($Mn_{interlayer}$ and Me) were determined by XRD and EXAFS spectroscopy (Table 1). The combined use of XRD (Lanson et al. 2002a), SAED, EDA (present article), and EXAFS spectroscopy (Manceau et al. 2002) provides new insight not only into the structural and chemical features of these MeBi, but also into the structural mechanism of formation as a result of the equilibration of high-pH NaBu at low pH in the presence of heavy metal cations.

EXPERIMENTAL METHODS

The birnessite samples studied in the present article are those described in the two companion papers (Lanson et al. 2002a;

Manceau et al. 2002), and their chemical compositions are given in Table 1 of Lanson et al. (2002a). In the following, they will be denoted according to their Me/Mn ratios (e.g., ZnBi 122 standing for a 0.122 Zn/Mn ratio). Aliquots from diluted suspensions were dried onto carbon-coated copper or aluminum grids. The samples were then mounted on a tilting sample holder. SAED patterns were recorded using either a JEOL JEM100c equipped with a Kevex X-ray spectrometer and operated at 100 kV or a Philips CM300ST equipped with a Kevex spectrometer system for energy-dispersive analysis (EDA) and operated at 300 kV. The standards used for the semi-quantitative EDA were $SrCuO_2$, Y_2BaCuO_5, $LaMnO_3$, La_2CuO_4, and $BaPbO_3$.

RESULTS

Features of SAED patterns

The different types of SAED patterns observed for the various birnessite samples are shown in Figures 1–5, and will be referred to hereafter as types I, II, III, IV, and V, respectively. All patterns contain a set of strong $hk0$ reflections distributed with hexagonal symmetry, which can be indexed either with a base-centered ($b^* = \sqrt{3}a^*$ and $\gamma^* = 90°$) or with a hexagonal ($a_H^* = b_H^* = 2a^*$ and $\gamma^* = 60°$) unit cell. In direct space, these cells correspond to a base-centered cell with $a = \sqrt{3}b$ and $\gamma = 90°$, or to a hexagonal cell $a_H = b_H = b$ and $\gamma = 120°$, respectively, as determined by XRD (Lanson et al. 2002a).

SAED patterns of type I. As can be seen in Figures 1a and 1b, each sub-cell reflection is surrounded by six weak super-cell reflections of similar intensity that form three pairs rotated with respect to each other by 120° around a vertical axis passing through the corresponding sub-cell reflection. The super-cell reflections are connected by three horizontal twofold axes (or vertical mirror planes) passing through the center of the SAED pattern and parallel to $[10]^*$, $[11]^*$, and $[1\bar{1}]^*$. Alternatively, the six super-cell reflections surrounding each sub-cell reflection may be split into two triplets (solid and open circles on Fig. 1b), the apices of which form an equilateral triangle. The two triplets, which correspond to twinned structural components, are rotated with respect to each other by 21.79° around a vertical axis passing through the sub-cell reflection. The sides of the triangles are parallel to $[91]^*$, $[6\bar{4}]^*$, and $[35]^*$ for the first one (irregular dashed line), and to $[9\bar{1}]^*$, $[64]^*$, and $[3\bar{5}]^*$ for the second one (regular dashed line). Along any of these six directions, super-cell reflections are regularly spaced by $2b^*/\sqrt{7}$. For example, along $[6\bar{4}]^*$, the distance between two $hk0$ reflections ($2\sqrt{7}b^*$) is divided into 7 intervals (Fig. 1c).

The distribution of super-cell reflections aligned along $[91]^*$, $[6\bar{4}]^*$, and $[35]^*$ may be described by a supercell with $A_{or}^* = b^*/\sqrt{7}$, $B_{or}^* = \sqrt{3}b^*/\sqrt{7}$, and $\gamma^* = 90°$ (Fig. 1c). $\mathbf{A}_{or}^*$ and $\mathbf{B}_{or}^*$ are rotated by 10.89° with respect to $\mathbf{a}^*$ and $\mathbf{b}^*$, respectively. Alternatively, this distribution may be described by a hexagonal cell with $A_H^* = B_H^* = 2A_{or}^* = 2b^*/\sqrt{7}$ and $\gamma^* = 60°$ (Fig. 1c). The $\mathbf{A}_H^*$ and $\mathbf{a}^*$ axes also form a 10.89° angle. In direct space, these cells correspond to the base-centered cell $A_{or} = \sqrt{7}b$, $B_{or} = \sqrt{7}b/\sqrt{3}$, and $\gamma = 90°$, and to the hexagonal cell $A_H = B_H = \sqrt{7}b/\sqrt{3}$, and $\gamma = 120°$, respectively. The distribution of super-cell reflections along $[9\bar{1}]^*$, $[64]^*$, and $[3\bar{5}]^*$ is characterized by the same su-

TABLE 1. Main structural features of MeBi as determined from XRD and EXAFS results (Lanson et al. 2002a; Manceau et al. 2002)

Sample	Layer stacking	Well-defined stacking faults	Location and coordination of interlayer cations		
			$Mn_{interlayer}$	Me	Add. Me
ZnBi 69	1M (+**a**/3)	1H	–	–	–
ZnBi 122	1M (+**a**/3)	1H –12%	^{VI}TC sites above OR below	^{VI}TC sites above AND below	^{IV}TC sites above AND below
ZnBi 128	1M (+**a**/3)	1H –15%	^{VI}TC sites above OR below	^{VI}TC sites above AND below	^{IV}TC sites above AND below
PbBi 6	1H	1M (−**a**/3) – 2%	^{VI}TC sites above OR below	^{VI}TC sites above OR below	–
PbBi 58	1H	1M (−**a**/3) – 3%	^{VI}TC sites above OR below	^{VI}TC sites above OR below	^{VI}TE sites above OR below
CdBi 106	1H	1M (+**a**/3) – 8%	^{VI}TC sites above OR below	^{VI}TC sites above AND below	–
CuBi 156	–	–			–

Notes: In TC sites, Me is located above/below vacant layer octahedra and shares three O_{layer} with neighboring Mn_{layer} octahedra to form a triple-corner surface complex (Fig. 6 in Lanson et al. 2002a). In TE sites Me is located above/below empty tridentate cavities sharing three edges with Mn_{layer} octahedra (Fig. 8 in Lanson et al. 2002a). In the latter sites, coordination of Pb is always octahedral (^{VI}TE sites), whereas Me may be octahedral or tetrahedrally coordinated in TC sites. Add. indicates additional position for Me.
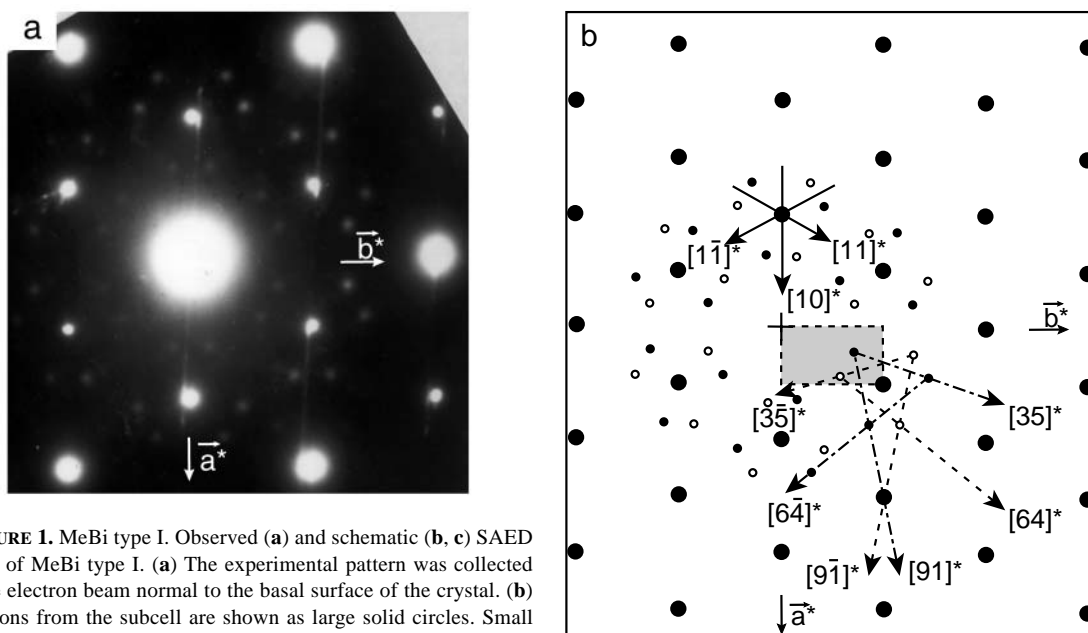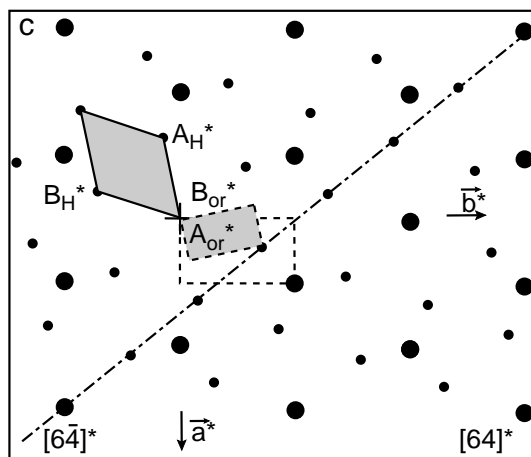

FIGURE 1. MeBi type I. Observed (**a**) and schematic (**b**, **c**) SAED patterns of MeBi type I. (**a**) The experimental pattern was collected with the electron beam normal to the basal surface of the crystal. (**b**) Reflections from the subcell are shown as large solid circles. Small circles represent reflections of the right-handed (solid circles = irregular dashed line) and left-handed (open circles = regular dashed line) supercells. The unit cell is shown as a gray rectangle. (**c**) For clarity, only the right-handed supercell is shown. Supercells are shown as gray rectangles. Orthogonal and hexagonal cells are outlined by dashed and solid lines, respectively.

per-cell parameters, the two supercells describing the two networks of super-cell reflections being connected by a mirror plane ($\mathbf{a}^*\mathbf{c}^*$).

As the two networks are twinned, the complete distribution of super-cell reflections observed in SAED patterns of type I can be described by a unique hexagonal supercell $A^* = B^* = 2a^*/7$ and $\gamma^* = 60°$, corresponding to the $A = B = 7b$ and $\gamma = 120°$ cell in direct space.

SAED patterns of type II. The distribution of strong sub- and weak super-cell reflections shown in Figure 2a is shown schematically in Figure 2b. Each sub-cell reflection is surrounded by 12 super-cell reflections that form six pairs rotated with respect to each other by 60° around a vertical axis passing through the sub-cell reflection. Alternatively, these super-cell
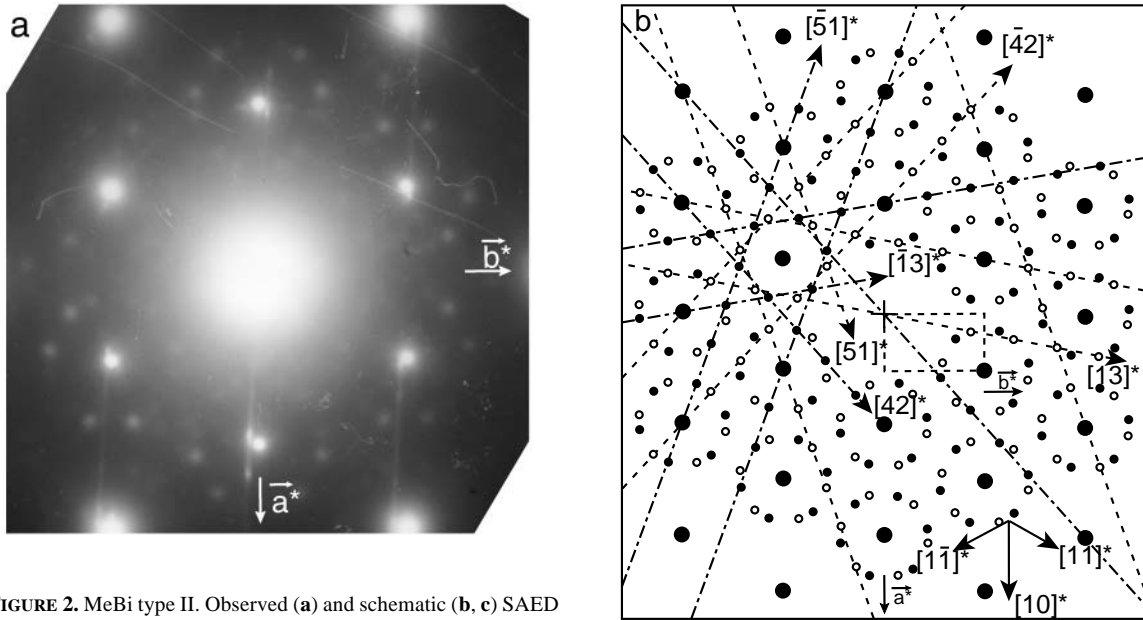
FIGURE 2. MeBi type II. Observed (**a**) and schematic (**b**, **c**) SAED patterns of MeBi type II. All symbols as in Figure 1.

reflections can be grouped in two hexagons rotated with respect to each other around the same vertical axis by 21.79° (solid and open circles; Fig. 2b). The sides of the first hexagon are parallel to $[\bar{5}1]^*$, $[\bar{1}3]^*$, and $[42]^*$ (irregular dashed line; Fig. 2b), whereas the sides of the second are parallel to $[51]^*$, $[13]^*$, and $[\bar{4}2]^*$ (regular dashed line; Fig. 2b). Super-cell reflections are distributed along each of these directions, with a period equal to $2a^*/\sqrt{7}$.

The network of super-cell reflections distributed along $[\bar{5}1]^*$, $[\bar{1}3]^*$, and $[42]^*$ may be described by a hexagonal $A_H^* = B_H^* = 2a^*/\sqrt{7}$ and $\gamma^* = 60°$, or an orthogonal $A_{or}^* = a^*/\sqrt{7}$, $B_{or}^* = b^*/\sqrt{7}$, and $\gamma^* = 90°$ supercell (Fig. 2c). The $\mathbf{A}_H^*$ and $\mathbf{A}_{or}^*$ axes are parallel to $[\bar{5}1]^*$ and are rotated with respect to the $\mathbf{a}^*$ axis by 19.11° around a common origin. In direct space, these cells have the following parameters: $A_H = B_H = \sqrt{7}b$ and $\gamma = 120°$, and $A_{or} = \sqrt{7}a$, $B_{or} = \sqrt{7}b$, and $\gamma = 90°$, respectively. Super-cell reflections distributed along $[51]^*$, $[13]^*$, and $[\bar{4}2]^*$ also form a hexagonal network with the same super-cell parameters, the supercells corresponding to the two networks being connected by a mirror plane passing through the $\mathbf{a}^*$-$\mathbf{c}^*$ plane. All super-cell reflections of the twinned supercells may be described using a common supercell with $A_{or} = 7a$, $B_{or} = 7b$, and $\gamma = 90°$, or $A_H = B_H = 7b$ and $\gamma = 120°$ in direct space.

SAED patterns of type III. In contrast to all other SAED patterns, the type-III varieties contain weak sub-cell reflections with $h + k = 2n + 1$ (Fig. 3a), which indicates that these crystals have a primitive rather than a base-centered unit cell. In addition, along the $\mathbf{a}^*$ axis, there is a weak super-cell reflection between any pair of sub-cell reflections, both intense and weak ones. These weak super-cell reflections are almost equidistant from the two sub-cell reflections, and careful measurement has shown that they are regularly spaced by $a^*/2.15$ (Fig. 3b), meaning that the periods of the sub- and super-cells are incommensurate along the $\mathbf{a}$ axis. The super-cell parameters are $A = 2.15$

a, $B = b$, and $\gamma = 90°$ in direct space.

SAED patterns of type IV. These patterns also are characterized by an incommensurate distribution of super-cell reflections along the $\mathbf{a}^*$ axis. The interval between two successive sub-cell reflections is divided into five almost equal intervals by four super-cell reflections (Fig. 4a). Careful measurement of these intervals has shown that the distance between two nearest super-cell reflections is slightly smaller than $2a^*/5$ and is actually equal to $2a^*/5.25$. All super-cell reflections can be described using a supercell with $A_{or}^* = a^*/5.25$, $B_{or}^* = b^*$ and $\gamma^* = 90°$, corresponding to the $A_{or} = 5.25\ a$, $B_{or} = b$, and $\gamma = 90°$ base-
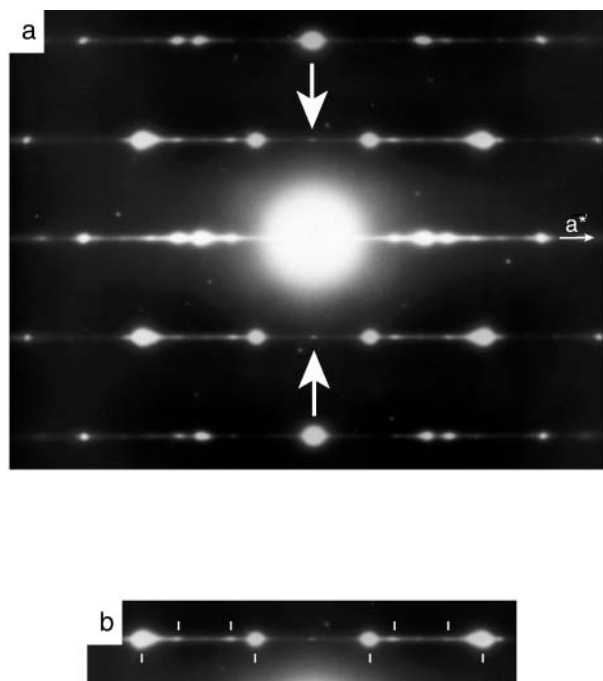
FIGURE 4. MeBi type IV. Observed (**a**, **b**) SAED patterns of MeBi type IV. (**b**) Ticks indicate the positions of sub- and super-cell reflections (below and above reflections, respectively) to allow for an accurate determination of the super-cell periodicity ($A^* = a^*/5.25$).

FIGURE 3. MeBi type III. Observed (**a**, **b**) SAED patterns of MeBi type III. (**a**) Large arrows indicate the faint sub-cell reflections with $h + k = 2n + 1$. (**b**) Ticks indicate the positions of sub- and super-cell reflections (below and above reflections, respectively) to allow for an accurate determination of the super-cell periodicity ($A^* = a^*/2.15$).

centered unit cell in direct space. Because the value of A_{or} is close to $5a$, sub- and super-cell reflections coincide at low h values, whereas at higher h values positions of these reflections are further away resulting in elongated spots (Fig. 4b).

SAED patterns of type V. SAED patterns of this type contain only sub-cell reflections distributed according to hexagonal symmetry (Fig. 5).

Occurrence of the different types of SAED patterns

Individual particles of each sample, depending mostly on the identity and amount of Me, have different SAED patterns. For example, Table 2 shows that SAED patterns of CuBi and PbBi 6 are exclusively of type V, whereas all types of SAED patterns occur for ZnBi 69 crystals. More generally, SAED patterns with a two-dimensional (2D) super-cell periodicity (types I and II) were observed only for ZnBi crystals; type III was present in ZnBi 69, PbBi 58, and CdBi 106; and type IV in ZnBi 69 and CdBi 106. Finally, SAED patterns of type V occur in all samples, being prevalent or abundant in PbBi 6 and 58, CdBi 106, and CuBi 156.

EDA results

Relative proportions of Me, Mn, and Na, as determined from EDA in each type of micro-crystal previously identified by
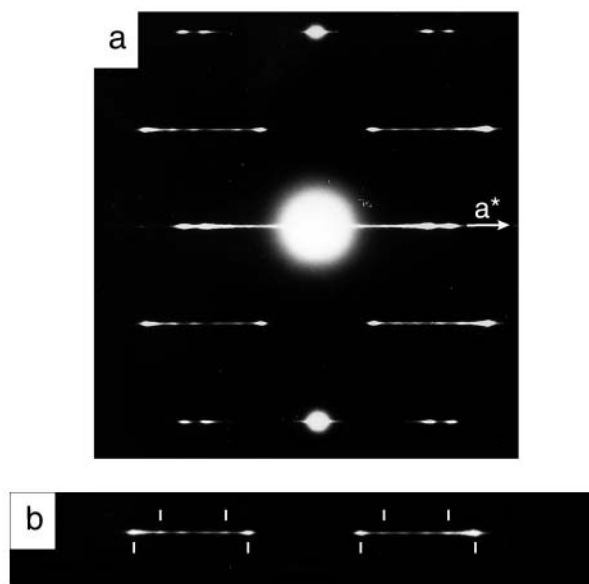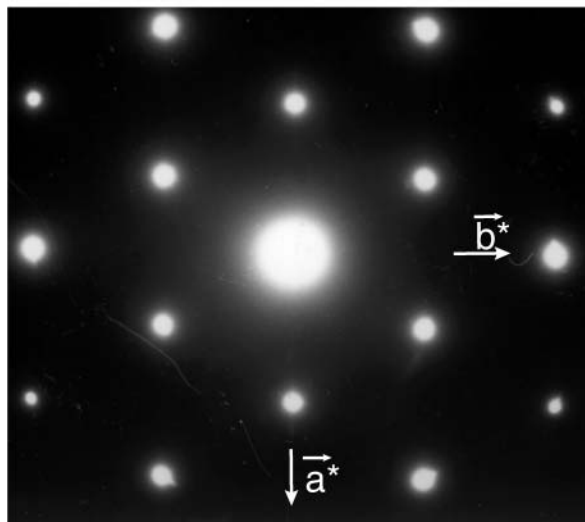

FIGURE 5. MeBi type V. Observed SAED pattern.

SAED, are reported in Table 3. This table shows that the type of SAED pattern depends on the Me/Mn ratio for ZnBi, CdBi, and PbBi micro-crystals. In particular, this ratio decreases in the sequence of SAED type II > I > IV > III in ZnBi micro-crystals, V > IV > III in CdBi micro-crystals, and IV > V in PbBi micro-crystals. The Me/Mn ratios obtained from EDA are close to those calculated from chemical analysis (Lanson et al. 2002a) if the EDA values obtained for PbBi, CdBi, and ZnBi 69 micro-crystals showing different types of abundant

TABLE 2. Occurrence of the different types of SAED patterns for the various samples

Sample	SAED Type I	SAED Type II	SAED Type III	SAED Type IV	SAED Type V
ZnBi 69	++	+	±	++*	+
ZnBi 122	–	+++	–	–	+†
ZnBi 128	–	+++	–	–	+†
PbBi 6	–	–	–	–	+++
PbBi 58	–	–	++	–	++†
CdBi 106	–	–	±	++	++
CuBi 156	–	–	–	–	+++†

Note: +++, ++, +, ±, – for prevalent, abundant, accessory, seldom observed, not observed.
* Some SAED patterns of type IV were rotated with respect to each other by 120° around a common origin (not shown).
† Some of the SAED patterns of type V were rotated with respect to each other by 21.79° around the center of the electron diffraction pattern (not shown).

TABLE 3. EDA analyses calculated as atomic ratios as a function of SAED type for the various samples

Sample	SAED Type	Me	Mn	Na	Me/Mn (EDA)	Me/Mn (Chem.)
ZnBi 122	II	10.7	89.3	–	0.122	0.122
ZnBi 69	I	7.7	92.3	–	0.083	
ZnBi 69	IV	4.6–5.5	94.5–95.4	–	0.048–0.058	0.069
ZnBi 69	III	3.70	96.3	–	0.038	
CdBi 106	V	13.3–13.4	86.6–86.7	–	0.154	
CdBi 106	IV	7.5	92.5	–	0.081	0.106
CdBi 106	III	6.5	93.5	–	0.070	
PbBi 58	III	6.3	93.7	–	0.067	0.058
PbBi 58	V	3.9	91.5	4.6	0.043	
CuBi 156	V	12.8	87.2	–	0.147	0.156

SAED patterns (types III and V, IV and V, and I and IV, respectively) are averaged with equivalent weights.

INTERPRETATION

As discussed by Drits et al. (1998) for birnessite samples synthesized at high pH, super-cell reflections originate from the ordered distribution of interlayer cations and associated H_2O molecules. For birnessite samples equilibrated at low pH, this arrangement likely depends on both the total layer charge and the distribution of negative charges within layers, that is, on the ordering of heterovalent Mn cations and of vacant layer sites. The presence of such vacant layer sites capped by interlayer cations has been demonstrated in the studied samples by XRD and EXAFS (Table 1; Lanson et al. 2002a; Manceau et al. 2002).

SAED patterns of type I

This type of SAED pattern was observed only in ZnBi 69 (Table 2). To determine the positions of Zn in the interlayer of this structure, let us consider the 2D distribution of lattice nodes in one of the two twinned networks. According to XRD (Lanson et al. 2002a), adjacent layers in ZnBi are predominantly shifted with respect to each other by $+\mathbf{a}/3$. Figure 6 shows the mutual arrangement of Mn cations belonging to two adjacent layers in projection along the $\mathbf{c}^*$ axis. Taking the origin of the hexagonal unit cell in a Mn site of the lower layer, the nodes of the hexagonal supercell ($A_H = B_H = \sqrt{7}b/\sqrt{3} = 4.350$ Å and $\gamma = 120°$; regular dashed line, Fig. 6) coincide with three structurally different octahedral sites as the $\mathbf{A}_H$ axis is rotated with respect to the $\mathbf{a}$ axis by 19.11°, in agreement with the mutual orientation
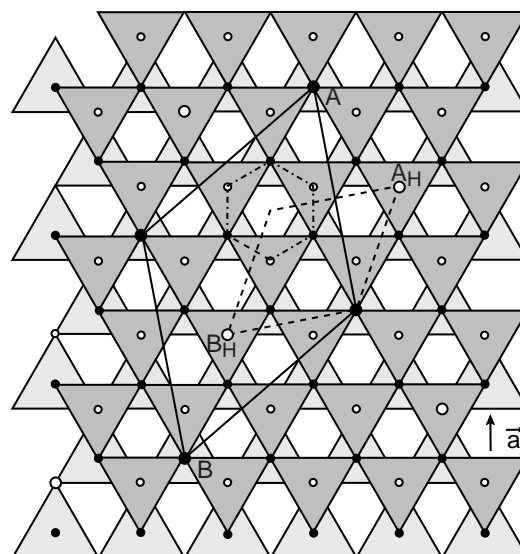

FIGURE 6. 2D distribution in projection on the **a-b** plane of lattice nodes corresponding to the super-cell reflection distribution in one of the twin networks present in SAED patterns of type I. Adjacent layers are translated by $c \cdot \cos\beta = +0.333a$ along the **a** axis according to XRD data (Lanson et al. 2002a). Small circles represent Mn_{layer} from the lower (solid circles) and upper (open circles) layers defining the interlayer space. The upper surface of the lower layer, and the lower surface of the upper layer are shown as light and dark shaded triangles, respectively. O_{layer} are not shown. The regular dashed line outlines the hexagonal supercell. The nodes of this cell are located above a vacant octahedron of the lower layer (large solid circles), below a vacant octahedron of the upper layer (large open circles), or in the center of an octahedron defined by Mn sites of the upper and lower layers (irregular dashed line). A solid line outlines the hexagonal cell describing the distribution of Zn in one interlayer ($A = B = b\sqrt{7} = 7.536$ Å and $\gamma = 120°$).

of $\mathbf{A}_H^*$ and $\mathbf{a}^*$ (Fig. 1). Two of these sites (large solid and open circles; Fig. 6) coincide with positions of layer Mn cations (Mn_{layer}) from the upper and lower layers, whereas the third one is located in the center of a hexagon formed by Mn_{layer} of the upper and lower layers (irregular dashed line; Fig. 6). As a consequence, within each interlayer, Zn may occupy only two of the three available lattice nodes, because XRD and EXAFS showed that Zn forms triple-corner surface complexes (TC sites; Fig. 7 in Lanson et al. 2002a) above/below vacant Mn_{layer} sites by sharing three layer oxygen atoms (O_{layer}). The first occupied node is located above a vacant octahedron of the lower layer (large solid circle; Fig. 6), the second below a vacant octahedron of the upper layer (large open circle; Fig. 6), and the third possible node is not occupied by Zn. As a result, within a given interlayer, Zn positions related to each layer define a hexagonal cell having $A = B = b\sqrt{7} = 7.536$ Å and $\gamma = 120°$ as in chalcophanite (Wadsley 1955; Post and Appleman 1988). Because of the superposition of Zn belonging to adjacent layers, the overall periodicity of Zn distribution does not coincide with the periodicity of Zn distribution within an individual layer described above.

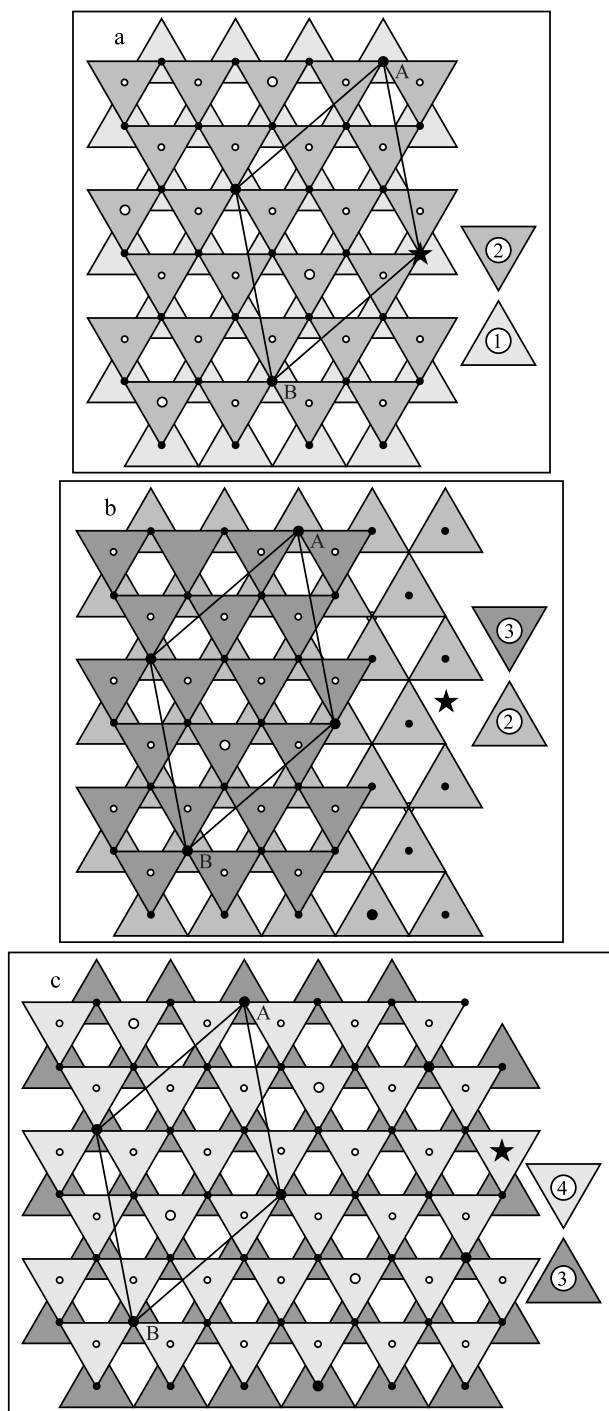To reconstruct the three-dimensional (3D) distribution of

FIGURE 7. 3D distribution in projection on the **a-b** plane of Zn in ZnBi 69 in one of the twin networks present in SAED patterns of type I. (**a**), (**b**), and (**c**) refer respectively to the first, second, and third interlayer regions of ZnBi type I. Symbols as in Figure 6, except for the shaded triangles, which correspond to the upper surface of the lower layer, and the lower surface of the upper layer, as illustrated on the right side of each Figure. The solid star indicates the origin in the first layer and is shown subsequently to indicate the total shift from that first layer. Layer 4 is equivalent to layer 1.

Zn in ZnBi 69, let us consider three adjacent interlayers formed by four successive layers labeled from 1 to 4 (Fig. 7). In the first interlayer (Figs. 6 and 7a), the Zn cations linked to layers 1 and 2 have coordinates (0,0) and ($A/3$, $2B/3$), respectively. To determine the position of Zn above layer 2, one must take into account the fact that Zn has to be located above and below vacant layer sites, in agreement with EXAFS and XRD results obtained for ZnBi 122 and 128 (Table 1). Furthermore, because Zn and Mn have similar scattering powers, the presence of Zn as pairs on each side of vacant layer sites is necessary to increase the electronic density of these sites as compared with that of occupied Mn_{layer} sites, and thus to induce significant intensity for super-cell reflections. As a consequence, Zn above layer 2 is also at ($A/3$, $2B/3$), Zn cations coordinated to each side of layer 3 have coordinates ($2A/3$, $B/3$), and the position of Zn cations linked to the fourth layer is (0,0), the same as those linked to layer 1 (Fig. 7c). Only such a distribution of Zn in successive interlayers allows preservation of the same unit cell for the whole crystal. This distribution implies a three-layer periodicity with $A = B = 7.536$ Å, $C = 3c = 21.18$ Å, $\alpha = \beta = 90°$, and $\gamma = 120°$. In projection along the $\mathbf{c}^*$ axis, Zn cations from successive interlayers occupy sites with coordinates (0, 0), ($A/3$, $2B/3$), and ($2A/3$, $B/3$) with equal probability, resulting in the reduced cell deduced from SAED patterns. This structure, corresponding to one of the twin networks, is identical to that of chalcophanite, which has a similar three-layer unit cell with $A = B = 7.53$ Å, $C = 3·6.93 = 20.79$ Å, and $\gamma = 120°$, and space group $R\bar{3}$ (Post and Appleman 1988). In this mineral, successive layers are shifted with respect to each other by 1/3 of the unit cell long diagonal.

However, in contrast to the chalcophanite structure described above, these ZnBi crystals are twinned, most likely as a result of a specific distribution of vacant octahedra in adjacent layers. When the vacant site of the lower layer is set at the unit cell origin, and the vacant site of the upper layer has coordinates ($A/3$, $2B/3$), vacant sites of the upper layer may be described by either one of the two hexagonal unit cells connected by a mirror plane **a-c** passing through the vacant site ($A/3$, $2B/3$; Fig. 8). The right-handed cell (regular dashed line) has the same orientation as that of the lower layer, whereas the left-handed cell (irregular dashed line) is rotated with respect to the right-handed one by 21.79° around a common origin ($A/3$, $2B/3$), so that the **A** axes of both cells form the same 10.89° angle with the **a** axis (Fig. 8). As a result, the complete distribution of super-cell reflections is described by the unique supercell with $A = B = 7b$ and $\gamma = 120°$, which is common to both right- and left-handed structural fragments. In addition to the 7 vacant layer sites from the lower layer (large solid circles), this supercell contains 7 vacant layer sites from the upper layer distributed according either to the right-handed (large open circles) or to the left-handed (large shaded circles) cell (Fig. 8). On Figure 8, note that the right-handed distribution of vacant layer sites in the upper layer allows the presence of Zn above and below each layer vacancy, as in this case Zn sites within the same interlayer are all far enough from each other to permit the formation of isolated Zn octahedra (large solid and open circles; Fig. 8).

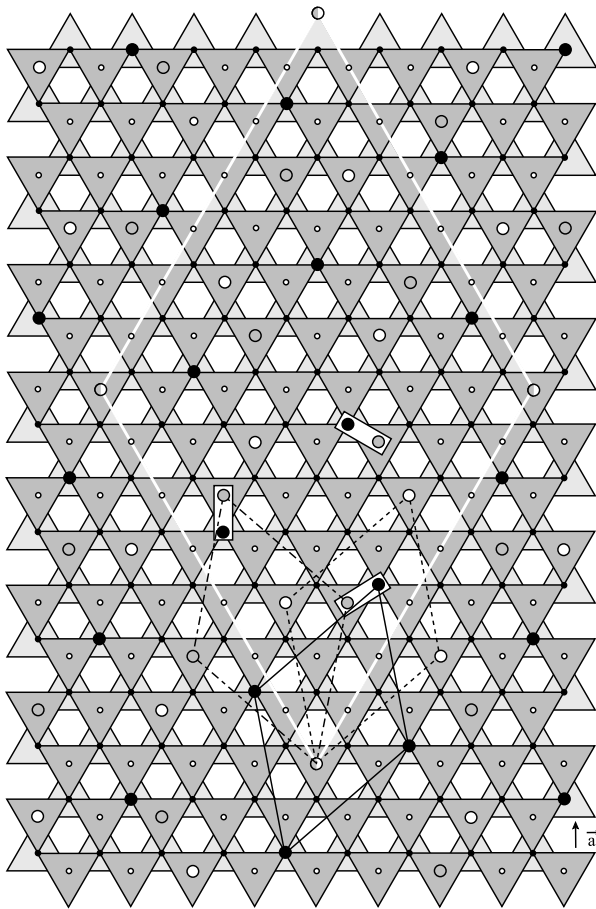In the alternative distribution of vacant octahedra described

FIGURE 8. 2D distribution in projection on the **ab**-plane of lattice nodes corresponding to the overall super-cell reflection distribution in the two twin networks of SAED pattern type of I. All symbols as in Figure 6, except where specified. The solid line outlines the right-handed supercell corresponding to the ordered vacancy distribution of the lower layer (large solid circles). The regular dashed line outlines the right-handed supercell corresponding to the ordered vacancy distribution of the upper layer (large open circles). The irregular dashed line outlines the left-handed supercell corresponding to the ordered vacancy distribution of the upper layer (large shaded circles). Vacant layer sites of the upper layer common to both right- and left-handed unit cells are shown as large half-and-half circles. The white line outlines the overall $A = B = 7b$ and $\gamma = 120°$ supercell common to both right- and left-handed structural fragments. Zn sites that may not be simultaneously occupied in an interlayer defined by layers whose vacant layer site distributions have different orientations are outlined by open boxes.

by the left-handed unit cell (large shaded circles; Fig. 8), three out of the seven available TC sites from the upper layer are too close to those from the lower layer for Zn to occupy the two sites simultaneously (Fig. 8). In addition to the short Zn-Zn distance (~3.1 Å), pairs of Zn cations located simultaneously in these two sites would share edges formed by H_2O molecules coordinated to Zn (H_2O_{Zn}) that cannot screen the electrostatic repulsion between the two Zn cations. Furthermore, in such a configuration, H_2O molecules coordinated by two Zn cations

would be strongly oversaturated because of the short Zn-H_2O_{Zn} distance (2.05–2.10 Å). To avoid such an unfavorable distribution of Zn in interlayers formed by successive layers having different distributions of vacant layer sites, Zn must be located either in the sites above the lower layer or in those below the upper one. In this case, solution protons may be sorbed to provide local charge compensation in vacant octahedra that are capped by Zn only on one side. In such interlayers the amount of Zn is decreased from 14 to 11, as three pairs of Zn positions cannot host Zn cations simultaneously. This modification of vacant layer site distribution between adjacent layers is likely not to be systematic, and right- and left-handed chalcophanite structural fragments probably alternate at random along the c^* axis. Each fragment may consist of several layers with the chalcophanite-like distribution of layer vacancies, Zn, and H_2O_{Zn}.

If adjacent layers having different distributions of vacant layer sites occur with the same probability in any micro-crystal, then the average thicknesses of right-handed and left-handed chalcophanite structural fragments are similar and their SAED patterns contain two equivalent super-cell reflection networks related by a mirror plane. However, according to simulation of XRD patterns and to chemical data (Lanson et al. 2002a), the above structural model is only a simplified scheme of the actual structure of ZnBi 69 crystals of type I, as Mn also occurs as an interlayer cation together with Zn. The possible distribution of Zn and Mn in ZnBi 69 interlayers will be described below.

SAED patterns of type II

This type of SAED pattern is overwhelmingly present in ZnBi 122 and 128 crystals and occurs less frequently in ZnBi 69 (Table 2). Figure 9 shows the mutual arrangement of Mn_{layer} in two adjacent ZnBi layers in projection along the c^* axis and the lattice nodes of the $A_H = B_H = b\sqrt{7} = 7.535$ Å and $\gamma = 120°$ unit cell describing super-cell reflections of one of the two networks. The origin of the unit cell is set to coincide with the center of a vacant octahedron from the lower layer (large solid circles; Fig. 9). As with crystals of type I, in ZnBi 69, the distribution of Zn located in TC sites in individual layers of type-II crystals is similar to that described for chalcophanite. In contrast, the distribution of vacant sites in adjacent layers of these type-II crystals differs substantially from that of chalcophanite. In the chalcophanite structure, the specific distribution of vacant sites in adjacent layers (Fig. 7) reduces the periodicity of the 2D lattice from $b\sqrt{7}$ to $b\sqrt{7}/\sqrt{3}$ (Fig. 6). In contrast, to preserve the 2D $b\sqrt{7}$ periodicity in projection along the c^* axis for the distribution of Zn, the vacant octahedron of the upper layer can be located in one of the three sites having coordinates (0.476, 0.381), (0.905, 0.524), and (0.619, 0.095) in the hexagonal cell (sites 1, 2, and 3, respectively; Fig. 9), in addition to the (1/3, 2/3) site. These sites are far enough from the nearest octahedral sites of the lower layer so as not to induce significant electrostatic repulsion of Zn cations coordinated to the two layers, and vacant layer octahedra may be capped by Zn on their two sides. In such a structure, each layer has the highest possible symmetry in projection along the c axis. However, the superposition of two successive layers dra-
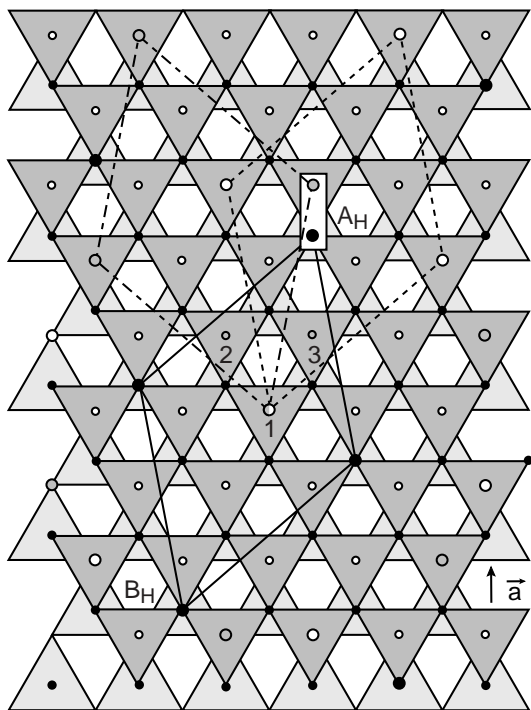
FIGURE 9. 2D distribution in projection on the **ab**-plane of lattice nodes corresponding to the overall super-cell reflection distribution in the two twin networks of SAED patterns of type II. Adjacent layers are translated by $c \cdot \cos\beta = +0.333 \, a$ along the **a** axis according to XRD data (Lanson et al. 2002a). All symbols as in Figure 8, except when specified. 1, 2, and 3 refer to the three possible positions for the origin of the unit cell describing the vacancy distribution of the upper layer to preserve the 2D $b\sqrt{7}$ periodicity, in projection along the **c** axis, for the distribution of Zn.

matically decreases their common symmetry, as the unit cell loses all elements of symmetry except for the translation along $\mathbf{A_H}$ and $\mathbf{B_H}$ (Fig. 9).

The structural model used to describe SAED patterns of type I may also be invoked to explain the twinning observed in SAED patterns of type II, and for a given distribution of vacancies in the lower layer, there are two possibilities for the vacancy distribution in the upper layer (Fig. 9). If vacancies of both layers possess the same azimuthal orientation (large solid and open circles, solid and regular dashed lines; Fig. 9), then Zn may systematically coordinate both sides of the vacant layer sites. In contrast, if vacancies of the lower and upper layers are respectively described by right- and left-handed cells (large solid and shaded circles, solid and irregular dashed lines; Fig. 9), possible TC sites for Zn are separated from each other either by short or by long distances. Interlayer sites separated by short distances cannot simultaneously host Zn because of electrostatic repulsion. As for SAED patterns of type I, the proposed model does not account for the significant amount of $Mn_{interlayer}$ present in ZnBi samples (Table 1); the possible distribution of Zn and $Mn_{interlayer}$ in these samples will be described below.

SAED patterns of types III and IV

To combine the observed incommensurate periodicity along the **a** axis with a periodic distribution of vacant layer sites capped by Me in a MeBi structure, two conditions must be fulfilled. The first is a proper mutual arrangement of adjacent layers. For example, a relative displacement of adjacent layers with respect to each other by $\pm\mathbf{a}/3$ is favorable for this incommensurate periodicity along the **a** axis. The second condition includes the periodic distribution of vacant sites within layers and from one layer to the adjacent one, with some specific limitations described below.

As an example, one may consider two adjacent layers shifted with respect to each other by $+\mathbf{a}/3$. To obtain an average periodicity of Me ordering equal to 2.25**a**, vacant octahedra may form pairs along the **a** axis within each layer, with vacant sites capped by Me being separated by $2a$ in each pair (Fig. 10). Vacancy pairs belong alternatively to the upper layer and to the lower layer and are distributed periodically along the **a** axis. If the first vacancy pair belongs to the lower layer (bottom of Figure 10a), the next one along the **a** axis belongs to the upper layer and is separated from the first one by $2.33a$ in projection along the $\mathbf{c}^*$ axis (Fig. 10). The third vacancy pair belongs again to the lower layer, and the distance between the nearest vacancies of the second and third vacancy pairs is $2.67a$ (Fig. 10). In such a distribution, the distance between the first and third vacancy pairs for the lower layer, as well as between the second and fourth pairs for the upper one, is $(2 + 2.33 + 2 + 2.67)a = 9a$, corresponding to four intervals between successive Me cations (Fig. 10). As a result, the average periodicity of the Me distribution along the **a** axis is equal to 2.25a. The measured 2.15a period can be obtained, within experimental precision, by assuming that the second and third pairs are separated by $2.67a$ or $1.67a$ with equal probability, as in this case the average Me periodicity is $[2 + 2.33 + 2 + (2.67 + 1.67)/2]a/4 = 2.125a$. Finally, if these one-dimensional (1D) sequences of vacancy pairs are distributed at random along the **b** axis, the subcell loses its base-centered property in projection along the $\mathbf{c}^*$ axis to become primitive. If these periodically distributed Me cations have octahedral coordination (Fig. 10b), water molecules coordinating these cations (H_2O_{Me}) form an empty octahedron with O_{layer} from the adjacent layer, thus forming weak H-bonds. In contrast, if Me is tetrahedrally coordinated (Fig. 10c), the short H_2O_{Me}-O_{layer} distance leads to the more favorable formation of strong H-bonds between adjacent layers, as discussed by Lanson et al. (2002a).

Similar diffraction effects can occur for 1H MeBi structures (e.g., PbBi 58; Table 2) if vacant layer sites are distributed periodically along the **a** axis, assuming that Me is not located in TC sites but rather is above or below empty tridentate cavities, sharing three edges with neighboring Mn_{layer} octahedra [TE sites, position (–0.333, 0); Fig. 8 in Lanson et al. 2002a]. For PbBi 58, the presence of Pb in this alternative position is consistent with the results obtained from XRD and EXAFS (Lanson et al. 2002a; Manceau et al. 2002). Figure 11 shows two adjacent layers in which pairs of Me cations located in TE sites are distributed along the **a** axis with $A_s = (2 + 2.67 + 2 + 2.33)a = 9a$ periodicity in projection along the $\mathbf{c}^*$ axis, yielding an average
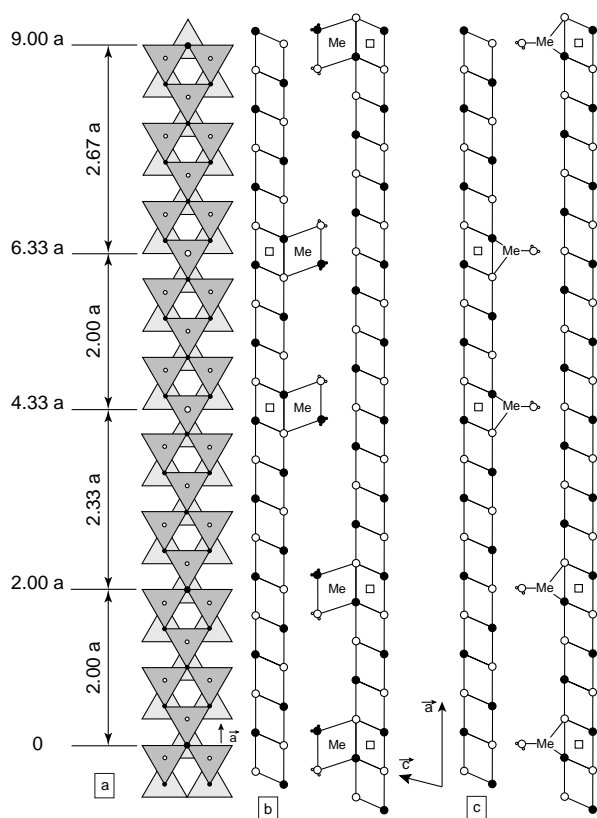
FIGURE 10. Possible distribution of vacant sites and associated Me leading to SAED patterns of type III for the 1M phase. Adjacent layers are translated by $c \cdot \cos\beta = +0.333$ a along the **a** axis. (**a**) Projection on the **ab**-plane. All symbols as in Figure 8. (**b**, **c**) Projection along the **b** axis. O_{layer} are shown as large circles. Open symbols indicate atoms at y = 0, and solid symbols indicate atoms at y = ±1/2. Vacant layer sites are shown as open squares, and Mn_{layer} is not shown. (**b**) Me is located above/below vacant layer sites and is octahedrally coordinated. (**c**) Me is located above/below vacant layer sites and is tetrahedrally coordinated.

FIGURE 11. Possible distribution of vacant sites and associated Me leading to SAED patterns of type III for the 1H phase. Adjacent layers are not translated along the **a** axis. (**a**) Projection on the **ab**-plane. All symbols as in Figure 8. Solid and open squares represent vacant layer sites from the lower and upper layers, respectively. (**b**) Projection along the **b** axis. All symbols as in Figure 10b. Me cations are located above/below empty tridentate cavities and are octahedrally coordinated.

2.25a periodicity. This period may be reduced to match the experimental one as for the 1M layer sequence.

A similar approach may be used to describe the $A = 5.25$ a periodic distribution of Me along the **a** axis (SAED patterns of type IV) for 1M microcrystals. Within each layer, pairs of vacant sites capped by Me are separated by 5a to match the observed period (Fig. 12). Because of the +**a**/3 relative displacement between adjacent layers, the distance between the nearest vacancies of the first and the second vacancy pairs is 5.33a whereas that between the second and third vacancy pairs is 5.67a, leading to an average 5.25a distance between Me cations (Fig. 12). To keep the base-centered symmetry of the $A = 5.25a$, $B = b$, and $\gamma = 90°$ supercell, sequences of vacancy pairs aligned along the **a** axis should be shifted by $(n\mathbf{A} + m\mathbf{b})/2$ (n and m being integers) with respect to each other. As a result, any interlayer 1D sequences of vacancy pairs having identical periodicity but shifted with respect to each other by $(\mathbf{A} + \mathbf{b})/2$ occur with equal probabilities and are interstratified at random
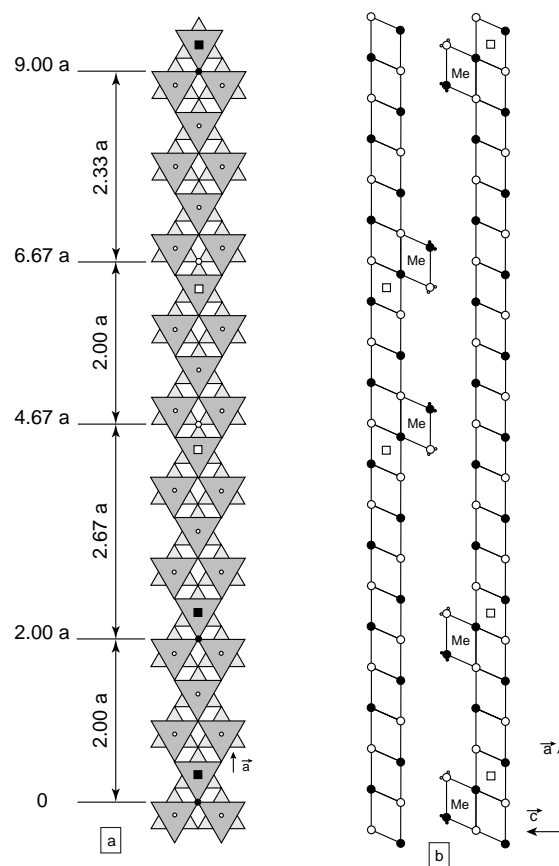
along the **b** axis.

Finally, the $A = 5.25$ a periodic distribution of Me is also encountered in some CdBi crystals that have a 1H layer stacking. The distribution of Cd in these crystals will be discussed below, as XRD showed that Cd is systematically present in ^{VI}TC sites (Table 1).

SAED patterns of type V

All crystals of CuBi, PbBi 6, and some of the other MeBi crystals exhibit SAED patterns of type V. Three hypotheses may account for the absence of super-cell reflections in these microcrystals. The first is the presence of Me having a scattering power similar to that of Mn located either above or below vacant layer octahedra. In this case, in projection along **c***, vacant and occupied octahedra have similar scattering power, and super-cell reflections are extremely weak or absent, even if Me cations are distributed periodically. This hypothesis is supported by the extremely weak super-cell reflections observed in the
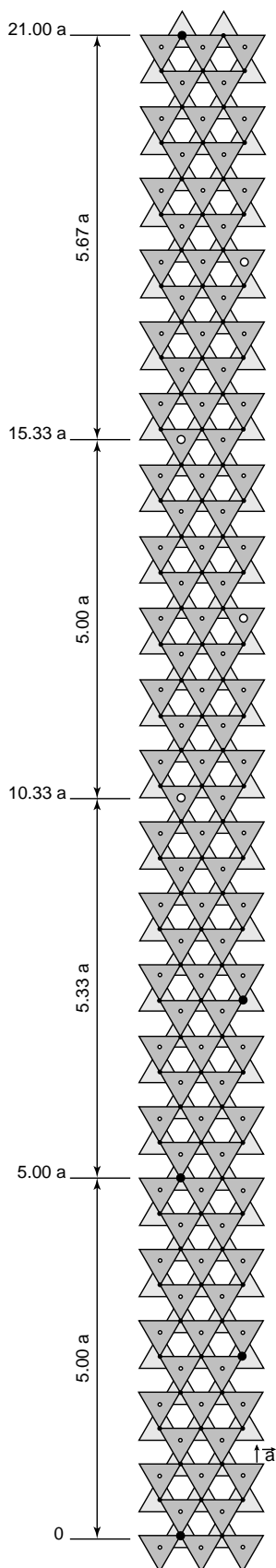
SAED patterns of HBi, in spite of the ordered distribution of vacant layer sites (Drits et al. 1997). This ordering may be the case for CuBi 156, because this sample contains a large amount of sorbed metal, a condition that seems likely to induce a periodic distribution of these cations within individual interlayers.

The second hypothesis is a low Me content, which can account for the absence of super-cell reflections in PbBi 6 because the low concentration of Pb (Pb/Mn = 0.006) is not conducive to long-range interactions. This hypothesis is supported by the SAED and EDA analysis of PbBi 58, which showed that microcrystals having a Pb/Mn ratio equal to 0.067 are characterized by type-IV SAED patterns whereas microcrystals with a lower Pb/Mn ratio (Pb/Mn = 0.043) exhibit type-V SAED patterns.

According to the third hypothesis, type-V SAED patterns result from a random distribution of Me cations, so that their average periodicity coincides with that of the layer, as in the case of CdBi. As the scattering power of Cd is significantly higher than that of Mn, strong super-cell reflections should arise from an ordered distribution of Cd, even if these cations were located either above or below vacant layer sites. This is the case for crystals of types III and IV, which are characterized by super-cell reflections along the **a** axis in spite of a low Cd content (Cd/Mn = 0.070–0.081). The absence of super-cell reflections in SAED patterns of crystals having a higher content of Cd (Cd/Mn = 0.154) can be considered as evidence for the random distribution of vacant sites among all available octahedral layer sites. The results of SAED pattern interpretation are summarized in Table 4 to show relationships between the structural diversity of the MeBi samples and the identity of Me.

DISCUSSION

Low-pH transformation of NaBu as a function of Me

In NaBu synthesized at high pH following the protocol of Giovanoli et al. (1970), the distribution of heterovalent Mn_{layer} is ordered, as Mn^{3+} cations are segregated into Mn^{3+}-rich rows parallel to [010] and separated from each other along the **a** axis by two Mn^{4+} rows. Because Mn^{3+} octahedra are elongated along the **a** axis, this ordered distribution violates the hexagonal layer symmetry and results in the formation of the $A = 3a$ supercell (Drits et al. 1997; Silvester et al. 1997; Lanson et al. 2002b). These authors, together with Lanson et al. (2000), showed that the transformation of NaBu to its low-pH form (HBi) involves two successive reactions. First, one third of $Na_{interlayer}$ is replaced by solution protons and one third of Mn^{3+}_{layer} disproportionates to form Mn^{4+}_{layer} and $Mn^{2+}_{solution}$, resulting in the formation of vacant layer sites. The second reaction includes the exchange of protons for the remaining Na and migration of half of the remaining Mn^{3+}_{layer} from layer to interlayer. As a result, the initially vacancy-free Mn^{3+}-rich rows consist of regularly alternating vacant and occupied layer octahedra in the HBi structure. In addition, at pH 4, about 0.04 Mn^{2+} re-adsorbs into the

◀ **FIGURE 12.** Possible distribution in projection on the **a-b** plane of vacant sites and associated Me leading to SAED patterns of type IV for the 1M phase. Adjacent layers are translated by $c \cdot \cos\beta = +0.333\ a$ along the **a** axis. All symbols as in Figure 8.

TABLE 4. Summary of MeBi structural varieties determined from SAED

MeBi varieties	Main structural features
- ZnBi 69 micro-crystals of type I	Twins of chalcophanite-like structural fragments - Vacant layer octa-hedra form a hexagonal unit cell with $A_H = \sqrt{7}b = 7.53$ Å - Octahedrally coordinated interlayer cations are located either above and below (Mn^{3+}) or above and below (Zn) vacant layer octahedra (^{VI}TC sites)
- ZnBi 69, 122, 128 micro-crystals of type II	Twins of ZnBi structural fragments - Individual layers have a chalcophanite-like distribution of vacant layer octahedra with $A_H = \sqrt{7}b = 7.53$ Å - In adjacent layers, these distributions are not regularly shifted with respect to each other by 1/3 of the long diagonal of the hexagonal layer unit cell ($A_H = \sqrt{7}b$) as in chalcophanite - Octahedrally coordinated interlayer cations are located either above and below (Mn^{3+}) or above and below (Zn) vacant layer octahedra (^{VI}TC sites)
- ZnBi 69 micro-crystals with a high ^{IV}Zn content - CdBi micro-crystals with a high content of 1M layer pairs	1M MeBi micro-crystals in which Me is only located above/below vacant layer octahedra (TC sites) - In projection along the c^* axis, pairs of Me cations form ordered 1D sequences along the **a** axis with pseudo-periods equal to 2.15 a (type III) or 5.25 a (type IV) - Me may be tetrahedrally (Zn) or octahedrally (Mn^{3+}, and Cd) coordinated
- PbBi 58	1H MeBi micro-crystals in which Me is partly located above/below empty tridentate cavities (^{VI}TE sites) - In projection along the c^* axis, pairs of Me cations form ordered 1D sequences along the **a** axis with pseudo-periods equal to 5.25 a (type IV).
- ZnBi 69, 122, 128, PbBi 58, CdBi - PbBi 6 - CuBi	MeBi micro-crystals with either - randomly distributed vacant layer sites and associated Me, or - a very low amount of Me, or - Me having a scattering power similar to Mn, and located either above or below vacant layer sites

interlayer (Silvester et al. 1997) leading to the formula: $H^+_{0.324}Mn^{3+}_{0.123}Mn^{2+}_{0.043}(Mn^{4+}_{0.722}Mn^{3+}_{0.111}\square_{0.167})O_2$. Equilibration of an NaBu suspension at pH 4 in the presence of aqueous Co^{2+} is also accompanied by a layer-to-interlayer migration of Mn^{3+} and by the subsequent replacement of Mn^{3+} by Co^{3+} (Manceau et al. 1997).

These results consistently indicate that during equilibration of NaBu under acidic conditions, Mn^{4+} is immobile and unreactive. In contrast, interpretation of SAED data has shown that, at least in the presence of aqueous Pb, Cu, Zn, and Cd, the low-pH transformation of NaBu induces the migration of Mn_{layer} into the interlayer from sites initially occupied by Mn^{3+} and Mn^{4+}. As an example, the distribution of Mn^{3+} and Mn^{4+} in the initial NaBu layer and that of Zn according to the chalcophanite unit cell (SAED types I and II; Figs. 8 and 9) are superimposed in Figure 13. In this case, only one-third of the octahedral layer sites linked to Zn were initially occupied by Mn^{3+}_{layer}. Moreover, the chalcophanite distribution of Zn prevents any further migration of Mn^{3+}_{layer} from the initial Mn^{3+}-rich rows. Indeed, such a migration of Mn^{3+}_{layer} would lead to the formation of a pair of edge-sharing vacant octahedra (not shown) and a pair of adjacent interlayer octahedra sharing a common edge (irregular dashed lines; Fig. 13).

Two alternative NaBu-to-ZnBi transformation mechanisms may account for such a distribution of vacant layer octahedra. In the first, both Mn^{3+}_{layer} and Mn^{4+}_{layer} can migrate to the interlayer with similar probability, inconsistently with the higher mobility of Mn^{3+}_{layer} observed by Manceau et al. (1997) and Lanson et

al. (2000). In addition, the migration of Mn^{4+}_{layer} seems unrealistic given the presence of a significant amount of Mn^{3+}_{layer}, because the departure of Mn^{3+}_{layer} releases the steric strain within the layers. The alternative hypothesis assumes electron transfer from Mn^{3+}_{layer} to the adjacent Mn^{4+}_{layer} and the subsequent migration of the reduced Mn^{3+}_{layer} into the interlayer. According to this hypothesis, the NaBu-to-ZnBi transformation may be described as a four-step reaction. The first step is the diffusion of Zn in the interlayer, the second is the migration of electrons from Mn^{3+}_{layer} to Mn^{4+}_{layer} to generate the distribution of Mn^{3+}_{layer} according to the chalcophanite unit cell. The third step is the migration of Mn^{3+}_{layer}, resulting in a regular distribution of vacant layer octahedra. The last step involves the sorption of Zn on the two sides of vacant layer sites, with a partial substitution of Zn for $Mn_{interlayer}$.

In crystals having type-III and type-IV SAED patterns, Me cations are distributed as pairs and are separated from each other by 2**a** or 5**a**, respectively, along the **a** axis. Such a distribution may be achieved only by changing the initial $A = 3a$ super-cell periodicity of Mn^{3+}_{layer} ordering.

Interlayer structure and layer stacking mode as a function of Me

XRD results (Table 1) showed that the +**a**/3 shift between adjacent layers prevails for ZnBi varieties, whereas 1H layer stacking is predominant in PbBi and CdBi. Examination of Table 4 shows that additional structural features of MeBi, such
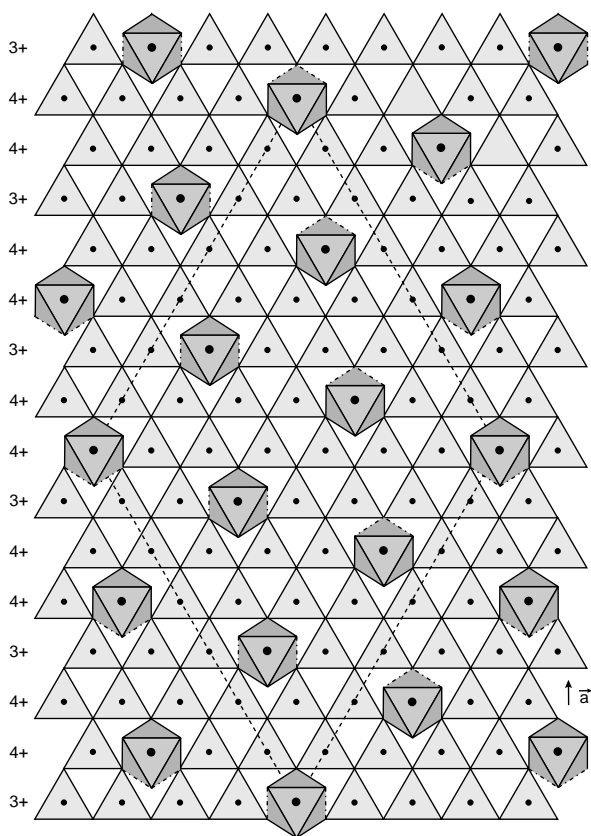
FIGURE 13. Possible distribution in projection on the **a-b** plane of vacant sites and associated Me leading to SAED patterns of types I and II. All symbols as in Figure 8, except for the dark shaded octahedra, which represent the octahedrally coordinated interlayer cations. 4+ and 3+ indicate the initial distribution of Mn^{4+} and Mn^{3+} cations in rows parallel to the **b** axis. Irregular dashed lines outline the edges that Me octahedra would share with Mn^{3+} in case of additional cation migration from the initial Mn^{3+}-rich rows.

as the distribution of newly formed vacant layer sites in the transformed NaBu structure, depend consistently on the identity of Me. For example, PbBi and CdBi are characterized by only 1D super-cell periodicities, whereas Zn induces either 1D or 2D ordering in the distribution of vacant layer octahedra and Zn. It is thus likely that the distribution of vacant layer sites and Me, the location and coordination of Me, and the mutual arrangement of adjacent layers are interdependent, as will be shown.

This mutual dependence may be illustrated at first for ZnBi micro-crystals of types I and II. In the 1M ZnBi structure, because of the +**a**/3 shift between adjacent layers, the three H_2O_{Zn} define an empty octahedron with the O_{layer} of the next layer, thereby forming weak H-bonds. In spite of this unfavorable configuration, the ordered chalcophanite-like distribution of vacant octahedra capped on each side by Zn (Figs. 8 and 9) strongly constrains the mutual arrangement of adjacent layers. Indeed, this distribution can occur only when adjacent layers are shifted with respect to each other by +**a**/3. This distribution

is compatible neither with the orthogonal layer stacking nor with the –**a**/3 1M stacking because, for these two layer stacking modes, the octahedral coordination of Zn by H_2O leads systematically to unrealistically short H_2O_{Zn}-H_2O_{Zn} distances (Fig. 14).

In ZnBi crystals of types III and IV (Figs. 10 and 12), adjacent layers are also shifted by +**a**/3 but the 1D ordering of Zn is totally different from the ordered chalcophanite-like distribution. To account for this apparent contradiction, one may note that together with $^{VI}Mn^{3+}$ and $^{VI}Zn^{2+}$, a significant amount of $^{IV}Zn^{2+}$ is present in ZnBi interlayers (Table 1). Because ^{VI}Zn should prevail in microcrystals with a chalcophanite-like distribution of Zn, it is possible to assume that 1D distributions of super-cell reflections observed for ZnBi micro-crystals (type-III and type-IV SAED patterns) correspond to 1M layer pairs that contain ^{IV}Zn or a mixture of ^{VI}Zn and ^{IV}Zn as interlayer cations. In this case, the short O_{layer}-H_2O_{Zn} distances permit the formation of strong H-bonds (Fig. 10c).

Similarly, two different configurations are possible for Pb located in TC or TE sites, and the ordered distribution along the **a** axis of Pb located in ^{VI}TE sites is likely responsible for the incommensurate 1D distributions of super-cell reflections observed for 1H PbBi 58 micro-crystals (Fig. 11). Such a location for Pb increases the distance between Mn_{layer} of one layer and Pb of the adjacent one, thereby decreasing their electrostatic repulsion as compared with the location of Pb in TC sites.

Finally, the origin of the 1D periodicity observed for 1H CdBi micro-crystals may be linked to the relatively high proportion of 1M layer pairs in the 1H stacking (Table 1). As a consequence, the 1M stacking mode may prevail in some CdBi crystals leading to the observed 1D super-cell periodicity (SAED patterns of type IV) if Cd^{2+} is distributed in ^{VI}TC sites as shown in Figure 10b.

Structural significance of Me/Mn ratios

The Me/Mn ratios determined by EDA for individual microcrystals having a 1D super-cell periodicity along the **a** axis may be used to calculate the frequency of the 1D Me sequences along the **b** axis. If $\overline{N}$**b** is the average separation between two adjacent sequences of Me, the primitive unit cell with $A = 2.15a$, $B = Nb$, and $\gamma = 90°$ contains 4.30N layer octahedra. One out of these $4.30\overline{N}$ layer sites is vacant and capped by one Me. As a consequence:

$$Me/Mn = 1/(4.3N–1). \qquad (1)$$

If the vacant octahedron is capped by Me on each side, then:

$$Me/Mn = 2/(4.3N–1). \qquad (2)$$

For the base-centered supercell with $A = 5.25a$, $B = Nb$, and $\gamma = 90°$, similar considerations transform Equations 1 and 2 to:

$$Me/Mn = 2/(10.5N–2) \text{ and } Me/Mn = 4/(10.5N–2),$$
respectively. $\qquad (3), (4)$

From Equation 1, N is equal to 3.7 for PbBi and CdBi microcrystals with $A = 2.15a$ and Me/Mn ≈ 0.07, that is, Me se-
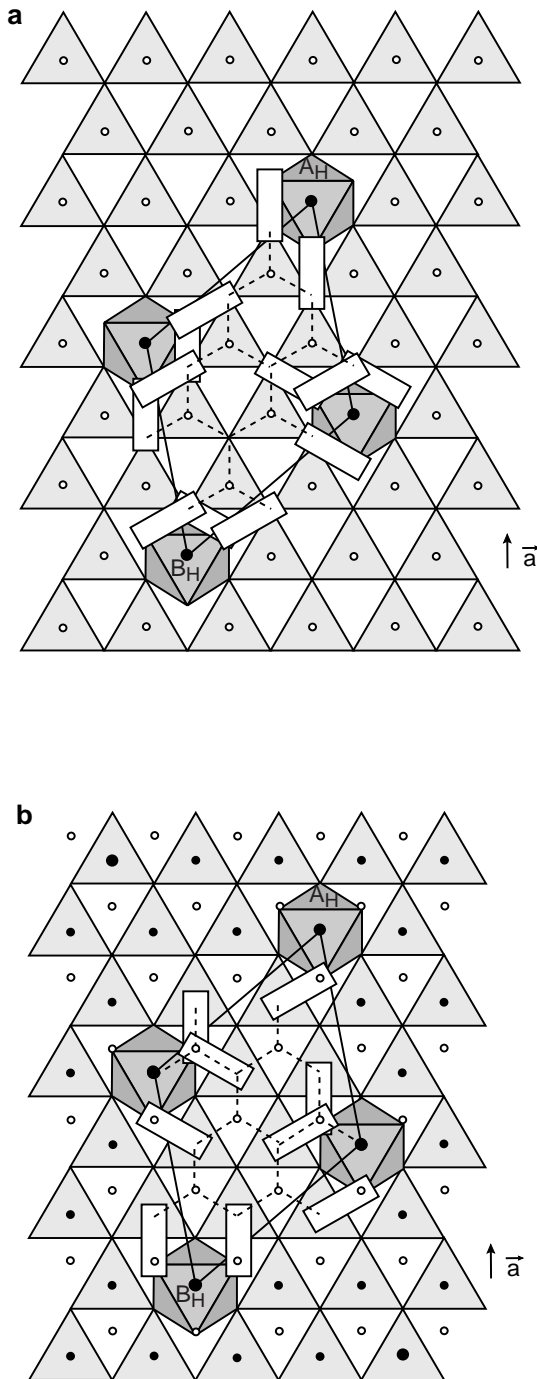
quences ordered along the **a** axis are repeated along the **b** axis every 3–4*b*. If Me cations coordinate the two sides of a vacant layer octahedron then N ≈ 7. Such an interval between two adjacent Me sequences is too long to provide a noticeable contribution to the intensity of observed super-cell reflections.

Similar conclusions may be drawn for CdBi microcrystals with $A = 5.25a$ and Cd/Mn = 0.08. In this case, Equation 3 leads to N ≈ 2.5, that is, the Cd sequences are repeated every 2–3*b* along the **b** axis. Again, location of Cd on only one side of a vacant layer octahedron looks preferable, as the presence of Cd on the two sides of the same vacant layer site would again lead to long distances between successive ordered Cd sequences. However, according to the structural formulae obtained from chemical and XRD results, Cd is located above and below vacant layer sites (Lanson et al. 2002a).

Application of Equations 1 and 3 to ZnBi microcrystals of types III and IV also leads to very long averaged intervals (~6.5**b** and ~4.2**b**) between successive ordered Zn sequences along the **a** axis regardless of whether Zn is sorbed on one or on two sides of vacant layer octahedra. Furthermore, because of the similar scattering powers of Zn and Mn, the presence of strong super-cell reflections in ZnBi SAED patterns with $A = 2.15a$ supports the occurrence of Zn on the two sides of vacant layer sites, in agreement with XRD results (Lanson et al. 2002a).

As shown above, the distance between Me sequences in MeBi crystals having type-III and type-IV SAED patterns is systematically too long to induce the observed strong super-cell reflections. A possible explanation for this apparent contradiction arising from the results obtained from chemistry, XRD, EDA, and SAED, lies in the existence of a dual reaction within the same micro-crystals during the NaBu-to-MeBi transformation. The first reaction leads to the formation of MeBi fragments with an apparent periodicity $A = 2.15\ a$ or $A = 5.25\ a$. In turn, the second reaction leads to the formation of HBi fragments containing mostly Mn^{3+} in interlayers. The coexistence within the same micro-crystals of these MeBi and HBi structural fragments is consistent with all of the observations.

Chemical composition and structural models of chalcophanite-like ZnBi crystals
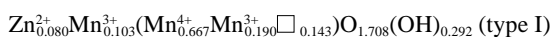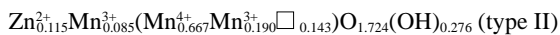
Chalcophanite and ZnBi have contrasting chemical compositions, with chalcophanite layers being built up of Mn^{4+} octahedra only (Post and Appleman 1988), but ZnBi layers containing both Mn^{3+} and Mn^{4+} together with vacant octahedra. This difference leads to contrasting layer charge between the two species and, as a result, to contrasting cation composition of their respective interlayers: chalcophanite interlayers contain only ^{VI}Zn, whereas Mn^{3+}, Zn^{2+}, and H^+ are present in ZnBi interlayers. To better assess both layer and interlayer cation compositions of these ZnBi crystals, one may assume that only Mn^{3+} have migrated from the layer as discussed above. As a result, 7 out of the 49 layer sites of the supercell common to the right- and left-handed chalcophanite unit cells ($A = B = 7b$ and $\gamma = 120°$) are vacant (Fig. 13), the other layer octahedra being occupied by Mn^{4+} (32.67) and Mn^{3+} (9.33). As vacant layer sites are capped on each side by Zn, the ideal composition of this supercell is: $Zn_{14}^{2+}(Mn_{32.67}^{4+}Mn_{9.33}^{3+}\square_7)O_{88.67}$ $(OH)_{9.33}$, or $Zn_{0.286}^{2+}(Mn_{0.667}^{4+}Mn_{0.190}^{3+}\square_{0.143})O_{1.810}(OH)_{0.190}$. The re-

FIGURE 14. Schematic 2D distribution in projection on the **ab**-plane of lattice nodes corresponding to the overall super-cell reflection distribution in the two twin networks of SAED patterns of type II. (**a**) Adjacent layers have 1H stacking. (**b**) Adjacent layers are translated by $c \cdot \cos\beta = -0.333\ a$ along the **a** axis. All symbols as in Figure 8, except for the dark shaded octahedral, which represent the octahedrally coordinated interlayer cations. Dashed lines outline the location of the three H_2O_{Me}, whereas open boxes outline unrealistically short distances between H_2O_{Me} from adjacent layers.

sulting Zn/Mn ratio of 0.333 is significantly higher than those determined experimentally (0.12 and 0.083 for type-II and type-I crystals, respectively; Table 3), and several hypotheses may be considered to decrease this ratio.

First, chalcophanite-like ZnBi crystals may have a mixed-layered structure consisting of both right- and left-handed chalcophanite fragments. As shown in Figure 8, if two adjacent layers have different orientations, only 11 of the 14 interlayer sites can be occupied simultaneously. As a result, a regular alternation of right- and left-handed chalcophanite fragments would lead to a $Zn_{11}^{2+}(Mn_{32.67}^{4+}Mn_{9.33}^{3+}\square_7)O_{82.67}$ $(OH)_{15.33}$, or $Zn_{0.224}^{2+}(Mn_{0.667}^{4+}Mn_{0.190}^{3+}\square_{0.143})O_{1.687}(OH)_{0.313}$ cation composition with a 0.262 Zn/Mn ratio.

According to the second hypothesis, two competing reactions take place in NaBu crystals during their low-pH transformation to ZnBi. These two reactions lead to the formation of either chalcophanite-like fragments or HBi fragments with Mn^{3+} as the unique interlayer cation. The coexistence of these two reactions is likely as, on the one hand, Mn^{3+} has a strong tendency to migrate from Mn^{3+}-rich rows at low pH to decrease steric strains and, on the other hand, the migration of electrons within the layers allows Mn_{layer} to migrate from layer sites initially occupied both by Mn_{layer}^{4+} and Mn_{layer}^{3+}. According to this second hypothesis, the Zn/Mn ratio is a function of the relative proportions of the two structural variants. For example, the coexistence in equal proportions of HBi and chalcophanite-like ZnBi fragments (respectively $Zn_{0.043}^{2+}Mn_{0.123}^{3+}$ $(Mn_{0.722}^{4+}Mn_{0.111}^{3+}\square_{0.167})O_{1.676}(OH)_{0.324}$, and $Zn_{0.286}^{2+}(Mn_{0.667}^{4+}$ $Mn_{0.190}^{3+}\square_{0.143})O_{1.810}(OH)_{0.190})$ leads to an average composition $Zn_{0.164}^{2+}Mn_{0.062}^{3+}(Mn_{0.694}^{4+}Mn_{0.150}^{3+}\square_{0.155})O_{1.744}(OH)_{0.256}$ and a Zn/Mn ratio of 0.181, closer to that determined experimentally for ZnBi microcrystals of type II (0.122).

The third hypothesis assumes that interlayer Zn and Mn are distributed randomly over the seven vacant octahedra of the supercell, Zn being located above and below vacant layer sites, whereas $Mn_{interlayer}$ is located either above or below these sites. In such a distribution, the numbers of vacant layer sites coordinated by two Zn cations (N) can be calculated from Zn/Mn = 2N/(49–N). Consequently, the numbers of vacant sites coordinated by interlayer Zn and Mn, respectively, should be 2.82 and 4.18 for microcrystals of type II (Zn/Mn = 0.122; Table 3) and 1.95 and 5.05 for microcrystals of type I (Zn/Mn = 0.083; Table 3). The following structural formulae may be calculated for these ZnBi microcrystals:

$$Zn_{0.115}^{2+}Mn_{0.085}^{3+}(Mn_{0.667}^{4+}Mn_{0.190}^{3+}\square_{0.143})O_{1.724}(OH)_{0.276} \text{ (type II)}$$

$$Zn_{0.080}^{2+}Mn_{0.103}^{3+}(Mn_{0.667}^{4+}Mn_{0.190}^{3+}\square_{0.143})O_{1.708}(OH)_{0.292} \text{ (type I)}$$

In this case, the interlayer cation composition of microcrystals of type II determined from SAED and EDA data is similar to that derived from the simulation of the experimental XRD pattern of ZnBi 122 ($Zn_{0.116}^{2+}Mn_{0.094}^{3+}$) for the same Zn/Mn ratio of 0.122. However, the amount of Mn^{4+} determined above for microcrystals of type II (0.667) is lower than that derived from XRD results for ZnBi 122 (0.722). The latter value originates from the structural model proposed by Silvester et al. (1997) for the NaBu-to-HBi transformation, which includes the initial
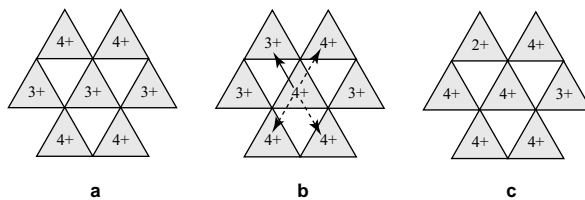

FIGURE 15. Schematic two-step reaction leading to a random distribution of Mn^{2+} and Mn^{3+} over the interlayer sites of the $A = B = 7b$ and $\gamma = 120°$ supercell (types I and II). All symbols as in Figure 8. Mn_{layer}^{4+}, Mn_{layer}^{3+}, and Mn_{layer}^{2+} are shown as 4+, 3+, and 2+, respectively. (**a**) Initial distribution of Mn^{3+} and Mn^{4+}. (**b**) Electron migration from a Mn^{3+} of the Mn^{3+}-rich row to one of the four adjacent Mn^{4+} (solid arrow). Migration to alternative Mn^{4+} sites are outlined by dashed arrows. (**c**) Disproportionation of the two adjacent Mn_{layer}^{3+}.

partial disproportionation of Mn^{3+} in Mn^{3+}-rich rows and the subsequent migration from layer to interlayer of Mn^{2+} and Mn^{3+}. In the supercell with $A = B = 7a$ and $\gamma = 120°$ (Fig. 13) determined for ZnBi micro-crystals of type II, which contain 32.67 Mn_{layer}^{4+} and 9.33 Mn_{layer}^{3+}, 2.33 of the 7 vacant layer sites were initially occupied by Mn^{3+}. If the initial disproportionation step is taken into account, the latter Mn cations may be reduced, leading to the migration of 2.33 Mn^{2+} to the interlayer and to an increased amount of Mn_{layer}^{4+} (32.67 + 2.33 = 35). The structural formula is then: $H_{16.33}^+Mn_{2.33}^{2+}Mn_{4.67}^{3+}(Mn_{35}^{4+}Mn_7^{3+}\square_7)O_{98}$, or $H_{0.333}^+Mn_{0.048}^{2+}Mn_{0.095}^{3+}(Mn_{0.714}^{4+}Mn_{0.143}^{3+}\square_{0.143})O_2$. If Mn^{2+} is subsequently replaced by Zn^{2+} located on each side of the vacant layer sites, this formula becomes: $H_{0.237}^+Zn_{0.096}^{2+}Mn_{0.095}^{3+}(Mn_{0.714}^{4+}Mn_{0.143}^{3+}\square_{0.143})O_2$.

Both layer and interlayer cation compositions of this formula are very close to those obtained from the simulation of XRD data. However, one may note that the systematic distribution of Zn pairs above and below vacant layer sites from initial Mn^{3+}-rich rows would lead to a $A = 3a$ super-cell periodicity along the **a** axis. This effect is minimized if disproportionation occurs after electron migration within the layers. Indeed, in the initial distribution of heterovalent Mn_{layer} cations, any Mn^{4+} row is adjacent to a Mn^{3+}-rich row along the **a** axis (Figs. 13 and 15a). As a consequence, electrons can migrate from a Mn_{layer}^{4+} to any adjacent Mn_{layer}^{4+} to form Mn^{3+}-Mn^{3+} pairs oriented along the **A** or **B** axes (Fig. 15b). Subsequent disproportionation enables the presence of Mn_{layer}^{2+} in any layer octahedron (Fig. 15c). As a consequence, such a random distribution of Mn^{2+} and Mn^{3+} over octahedral layer sites will lead to a random distribution of interlayer Zn-pairs and single Mn^{3+} after their migration from the layers and the substitution of Zn for Mn^{2+}. The above hypotheses account for the diffraction effects observed for ZnBi micro-crystals of types I and II, as well as for their layer and interlayer cation compositions.

prints of SAED micrographs. Steve Hillier kindly improved the English of an early version of this manuscript. Constructive remarks by David R. Veblen, Associate Editor David L. Bish, and an anonymous reviewer helped to improve the original manuscript.

REFERENCES CITED

Bendell-Young, L.I. and Harvey, H.H. (1992) The relative importance of manganese and iron oxides and organic matter in the sorption of trace metals by surficial lake sediments. Geochimica et Cosmochimica Acta, 56, 1175–1186.

Burns, R.G. and Burns, V.M. (1976) Mineralogy of ferromanganese nodules. In G.P. Glasby, Ed., Marine manganese deposits, p. 185–248. Elsevier, Amsterdam.

Chukhrov, F.V., Gorschkov, A.I., Rudnitskaya, E.S., and Sivtsov, A.V. (1978) Birnessite characterization. Investiya Akademie Nauk, SSSR, Seriya Geologicheskaya, 9, 67–76.

Drits, V.A., Silvester, E.J., Gorshkov, A.I., and Manceau, A. (1997) The structure of monoclinic Na-rich birnessite and hexagonal birnessite. Part 1. Results from X-ray diffraction and selected area electron diffraction. American Mineralogist, 82, 946–961.

Drits, V.A., Lanson, B., Gorshkov, A.I., and Manceau, A. (1998) Sub- and superstructure of four-layer Ca-exchanged birnessite. American Mineralogist, 83, 97–118.

Giovanoli, R., Stähli, E., and Feitknecht, W. (1970) Über Oxidhydroxide des vierwertigen Mangans mit Schichtengitter. 1. Mitteilung: Natriummangan(II,III)manganat(IV). Helvetica Chimica Acta, 53, 453–464.

Kuma, K., Usui, A., Paplawsky, W., Gedulin, B., and Arrhenius, G. (1994) Crystal structures of synthetic 7 Å and 10 Å manganates substituted by mono- and divalent cations. Mineralogical Magazine, 58, 425–447.

Lanson, B., Drits, V.A., Silvester, E.J., and Manceau, A. (2000) Structure of H-exchanged hexagonal birnessite and its mechanism of formation from Na-rich monoclinic buserite at low pH. American Mineralogist, 85, 826–838.

Lanson, B., Drits, V.A., Gaillot, A.-C., Silvester, E.J., Plançon, A., and Manceau, A. (2002a) Structural chemistry of heavy metal sorbed birnessite. Part 1: Results from X-ray diffraction. American Mineralogist, 87,1631–1645.

Lanson, B., Drits, V.A., Feng, Q., and Manceau, A. (2002b) Crystal structure determination of synthetic Na-rich birnessite: Evidence for a triclinic one-layer cell.

American Mineralogist, 87, 1662–1671.

Manceau, A., Gorshkov, A.I., and Drits, V.A. (1992) Structural Chemistry of Mn, Fe, Co, and Ni in Mn hydrous oxides. II. Information from EXAFS spectroscopy, electron and X-ray diffraction. American Mineralogist, 77, 1144–1157.

Manceau, A., Drits, V.A., Silvester, E.J., Bartoli, C., and Lanson, B. (1997) Structural mechanism of Co²⁺ oxidation by the phyllomanganate buserite. American Mineralogist, 82, 1150–1175.

Manceau, A., Lanson, B., Schlegel, M.L., Hargé, J.-C., Musso, M., Eybert-Bérard, L., Hazemann, J.-L., Chateigner, D., and Lamble, G.M. (2000) Chemical forms of trace metals in soils by XAFS spectroscopy. I. Quantitative Zn speciation in smelter-contaminated soils. American Journal of Science, 300, 289–343.

Manceau, A., Lanson, B., and Drits, V.A. (2002) Structure of heavy metal sorbed birnessite. Part 3: Results from powder and polarized EXAFS spectroscopy. Geochimica & Cosmochimica Acta, 66, 2639–2663.

McKenzie, R.M. (1967) The sorption of cobalt by manganese minerals in soils. Australian Journal of Soil Research, 5, 235–246.

——— (1980) The adsorption of lead and other heavy metals on oxides of manganese and iron. Australian Journal of Soil Research, 18, 61–73.

Post, J.E. and Appleman, D.E. (1988) Chalcophanite, ZnMn₃O₇·3H₂O: New crystal-structure determinations. American Mineralogist, 73, 1401–1404.

Post, J.E. and Veblen, D.R. (1990) Crystal structure determinations of synthetic sodium, magnesium, and potassium birnessite using TEM and the Rietveld method. American Mineralogist, 75, 477–489.

Silvester, E.J., Manceau, A., and Drits, V.A. (1997) The structure of monoclinic Na-rich birnessite and hexagonal birnessite. Part 2. Results from chemical studies and EXAFS spectroscopy. American Mineralogist, 82, 962–978.

Taylor, R.M. and McKenzie, R.M. (1966) The association of trace elements with maganese minerals in Australian soils. Australian Journal of Soil Research, 4, 29–39.

Wadsley, A.D. (1955) The crystal structure of chalcophanite, ZnMn₃O₇·3H₂O. Acta Crystallographica, 8, 165–172.